Journal of Industrial and Engineering Chemistry xxx (xxxx) xxx

Contents lists available at ScienceDirect

Journal of Industrial and Engineering Chemistry

journal homepage: www.elsevier.com/locate/jiec

Novel α-MnO_2/AC catalysts for heterogeneous catalytic ozonation process to remove BAA in dye wastewater

Cheng Gong [a], Xinxin Lv [a], Sheng Liu [a], Xing Chen [a,b], Rohan Weerasooriya [b], Zhaogang Ding [a,*]

[a] Key Laboratory of Nanominerals and Pollution Control of Higher Education Institutes, School of Resources and Environmental Engineering, Hefei University of Technology, Hefei 230009, PR China
[b] National Centre for Water Quality Research, National Institute of Fundamental Studies, Hantana, Kandy, Sri Lanka

ARTICLE INFO

Keywords:
Heterogeneous catalytic ozonation
MnO_2
Crystalline phase
Activated carbon
Bromamine acid

ABSTRACT

Designing catalysts that are both efficient and resistant to interference poses a significant challenge in the field of catalytic ozone oxidation. In this study, four composite nanomaterials with different crystalline phase structures of MnO_2 and its loading onto activated carbon were synthesized by hydrothermal synthesis-calcination method and successfully used to catalyze the degradation of BAA by ozonation. The synthesized α-MnO_2/AC showed excellent performance and stability, and the degradation rate of 100 mg/L BAA could reach 96.27 % within 40 min under optimal conditions. Compared with MnO_2 alone, α-MnO_2/AC possessed lower polarization resistance, faster charge transfer rate, and higher Mn^{3+} and oxygen vacancy contents. Through the mechanistic study of Heterogeneous catalytic ozonation (HCO), it was confirmed that Mn(III) and oxygen vacancies together acted as active sites to enable O_3 adsorption and activation to generate ROS, and $^{\bullet}OH$ and $^1O_2$ reacted with BAA as the main ROS in this system. In addition, a potential pathway for the degradation of BAA by HCO was proposed and evaluated for its toxicity. This study provides a new strategy and understanding for designing manganese dioxide composite catalysts with different crystalline phases and the mechanistic exploration of the HCO pathway.

Introduction

Rapid urbanization has led to the widespread use of synthetic dyes in various industries, including textiles, printing and dyeing, cosmetics, and many others [1]. The annual global dye production exceeds 600,000 tons, with over 50 % dedicated to textile dyeing. In the textile printing and dyeing processes, approximately 10 % to 20 % of dyes are discharged into water [2]. Anthraquinone dyes, known for their cost-effectiveness, ready availability, and excellent dyeing properties, are extensively employed as primary or secondary dyes in commercial tricolour dye formulations for cellulose textiles, wool, and polyamide fibies. This application enhances the dyeing outcomes, making anthraquinone dyes the second most utilized dyes, following closely behind azo dyes [3]. Bromamine Acid (1-Amino-4-bromoanthraquinone-2-sulfonic acid, BAA) is a crucial dye intermediate in synthesising anthraquinone-type dyes. It is water-soluble and commonly encountered in industrial wastewater, representing a class of recalcitrant, non-biodegradable organic pollutants. Due to the inefficient processes in dye production, substantial quantities of BAA are discharged into aquatic environments, posing significant environmental and health risks [4]. Due to the special anthraquinone structure of BAA, which contains −Br, –NH_2, and −SO_3H functional groups, and thus its biotoxicity, structural stability, and non-biodegradability, traditional biological methods cannot effectively treat this type of wastewater, and the search for an appropriate method for treating BAA wastewater is an urgent research need.

Advanced oxidation processes (AOPs) represent an effective technology for degrading recalcitrant organic pollutants in water. Among AOPs, ozone oxidation is a common process due to its powerful oxidizing ability and the absence of secondary pollution and many other advantages [5,6]. Among them, heterogeneous catalytic ozonation (HCO) has garnered significant attention due to its efficient mineralization of organic pollutants, wide pH applicability, and catalyst recyclability [7–9]. The nature of catalysts plays a pivotal role in determining the efficiency of heterogeneous catalytic ozonation (HCO). To enhance HCO efficiency, extensive research has been conducted to develop novel catalysts, such as metal oxides (e.g., manganese dioxide (MnO_2), iron oxide (FeOOH), and magnesium oxide (MgO)) [10–12]、Metal-free carbon materials, such as graphitic carbon nitride (g-C_3N_4), biochar, and graphene oxide [13–15]. Moreover, metal/metal oxide

* Corresponding author.
E-mail address: dzg@hfut.edu.cn (Z. Ding).

https://doi.org/10.1016/j.jiec.2024.06.044
Received 29 January 2024; Received in revised form 22 May 2024; Accepted 30 June 2024
Available online 2 July 2024

catalysts loaded onto carriers, such as Co-N@CNTs, are commonly employed [16], it is a commonly used catalyst. Among these, manganese oxides have been extensively investigated due to their high catalytic activity, ecological friendliness, and widespread natural dispersion. MnO_2 is widely employed for catalytic ozonation in manganese oxides, benefiting from its diverse oxidation states, varied structures, high stability, and cost-effectiveness. To date, various crystal forms of MnO_2, including α-, β-, γ-, and δ-MnO_2, as well as diverse morphologies such as linear, tubular, rod-shaped, and flower-shaped MnO_2, have been designed to achieve efficient catalytic ozonation [10,17–20]. The various crystal structures of MnO_2 have a profound effect on ozone catalyzed reactions. The special tunneling structure of MnO_2 has been reported to have a significant effect on the catalytic activity [21]. In addition, the prominent catalytic activity of MnO_2 may be related to its abundant oxygen vacancies [22]. The oxidizing activity of MnO_2 may also be related to the surface Mn(III) content [23]. Therefore, it is important to study and compare the characteristics of different crystalline phases of MnO_2 and their differences in performance for ozone-catalyzed degradation of pollutant.

However, using pure manganese oxides may lead to issues such as metal leaching and the aggregation of metal oxide nanoparticles in the solution, consequently affecting the efficiency of heterogeneous catalytic ozonation (HCO). The combination of manganese oxides with non-metallic materials could significantly improve the efficiency of HCO by suppressing the metal leaching problem, overcoming the high energy barrier from the reduction of $M^{(n+m)+}$ to M^{n+} (M, metal species) and preventing the agglomeration of ultrafine metal oxide nanoparticles in solution. For instance, Tian and colleagues reported the outstanding heterogeneous catalytic ozonation (HCO) activity of manganese-loaded biochar (MnOx/biochar) [24]. Xu et al. achieved the amino-functionalization hybridization of MnO_2 and graphene oxide (GO) and synthesized a heterogeneous solid catalyst, MnO_2-NH_2-GO, through a hydrothermal method. This catalyst was employed to degrade cefadroxil efficiently [25].Therefore, combining manganese oxides with non-metallic materials is be a promising approach for achieving excellent heterogeneous catalytic ozonation (HCO) performance. Against the backdrop of emphasizing carbon emissions and carbon sequestration, activated carbon emerges as an ideal non-metallic material due to its potential for solid waste recycling, carbon sequestration, and comprehensive greenhouse gas reduction, all at a low cost. Acknowledging the positive impacts arising from the interactions between heterogeneous Mn-based catalysts and carbonaceous materials, we suggest that the amalgamation of manganese oxide (MnO_2), known for its effective heterogeneous catalytic ozonation (HCO) capabilities, with carbonaceous materials like activated carbon, represents a viable strategy.

This study successfully loaded novel composite nanomaterials onto activated carbon with different crystalline phases of MnO_2 by a simple hydrothermal synthesis-calcination method. The composites were characterized by XRD, SEM, HRTEM, XPS and BET, and the performances of the different materials as catalysts for the degradation of BAA in HCO system were systematically compared. In addition, the reasons for the enhanced performance of α-MnO_2/AC as a catalyst in the HCO system and the effects of ozone concentration, pollutant concentration, experimental temperature and initial pH on the degradation efficiency of BAA were investigated, and the reactive oxygen species (ROS) generation and HCO mechanism were explored. Finally, the possible degradation intermediates of BAA and their acute toxicity were determined.

Materials and methods

Chemicals and reagents

The reagents and materials used are listed in Text S1.

Preparation of the catalyst

The α-, β-, γ- and δ-MnO_2 syntheses were adapted from previous reports [26,27] and their composites were prepared using an innovative approach. Details of catalyst preparation are presented in Supplementary Data Text.S2, and schematic diagram of the catalyst preparation is shown in Fig. S1.

Experimental methods

Using different crystalline phases of MnO_2 and MnO_2/AC as catalysts and Bromamine Acid (BAA) as a model pollutant, non-homogeneous ozone catalytic oxidation treatment was conducted on simulated wastewater in a glass gas-washing bottle with an effective volume of 500 mL. In the reactor, 200 mL of BAA solution was added, followed by an appropriate amount of catalyst. The system was placed in a 25℃-water bath and stirred continuously. Ozone, generated by a 3S-T10 laboratory ozone generator (Tonglin Technology, China), was bubbled into the bottom of the reactor at a flow rate of 500 mL/min through a diffuser. Subsequently, 2 mL of the reaction solution was extracted at predetermined intervals and filtered through a 0.45 μm nylon filter. Only the AC doping amount was varied when investigating the impact of AC doping on the catalytic performance of α-MnO_2/AC.

Ozone concentration was controlled by adjusting the voltage and measured using a 3S-J5000 desktop ozone concentration online analyzer (Tonglin Technology, China). The degradation efficiency of BAA was investigated under various conditions, including different catalysts, AC doping levels, catalyst dosages, ozone concentrations, initial pH values, different temperatures, and initial BAA concentrations. To assess the recyclability and stability of α-MnO_2/AC, particles were filtered and collected after each cycle, washed multiple times with ethanol and distilled water to remove residual organic compounds from the liquid film, and reused after drying at 60℃ for 8 h. Synthetic solutions were prepared using tap water and surface water and applied to actual wastewater samples to further explore the degradative capabilities of heterogeneous catalytic ozonation. All experiments were conducted in triplicate, and error bars represent the standard deviation of the mean.

Characterization

The characterization of the prepared catalysts involved are listed in Text S3.

Analytical method

The analytical method employed are shown in Text S4.

Results and discussion

Structural and morphological characterizations

The XRD spectra of α-, β-, γ- and δ-MnO_2 are shown in Fig. 1(a). α-, β-, γ- and δ-MnO_2 diffraction peaks match well with the diffraction peaks of α-MnO_2 (JCPDS 29-1020), β-MnO_2 (JCPDS 24-0735), γ-MnO_2 (JCPDS 14-0644) and δ-MnO_2 (JCPDS 80-1098) have well-matched diffraction peaks, which are consistent with the results of previous studies [18,20,28,29]. In Fig. 1(b), different stages of catalyst synthesis after doping with activated carbon (AC) are depicted. MnO_x/AC reveals new peaks corresponding to β-MnO_2. Conversely, activated carbon-doped forms of other manganese oxides α-MnO_2/AC, γ-MnO_2/AC, and δ-MnO_2/AC maintain identical diffraction peaks as their respective manganese dioxide phases. This observation is conclusive evidence for the successful synthesis of α-MnO_2/AC, γ-MnO_2/AC, and δ-MnO_2/AC in the current experiment.

According to scanning electron microscopy (SEM) shown in Fig. 2(a)

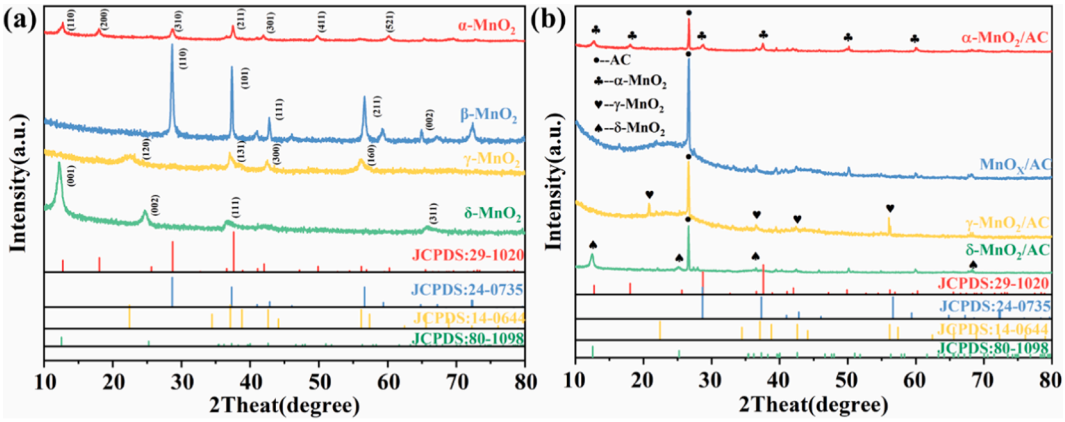

Fig. 1. XRD patterns of (a) Different crystalline phases of MnO_2, (b) Different composite nano materials.

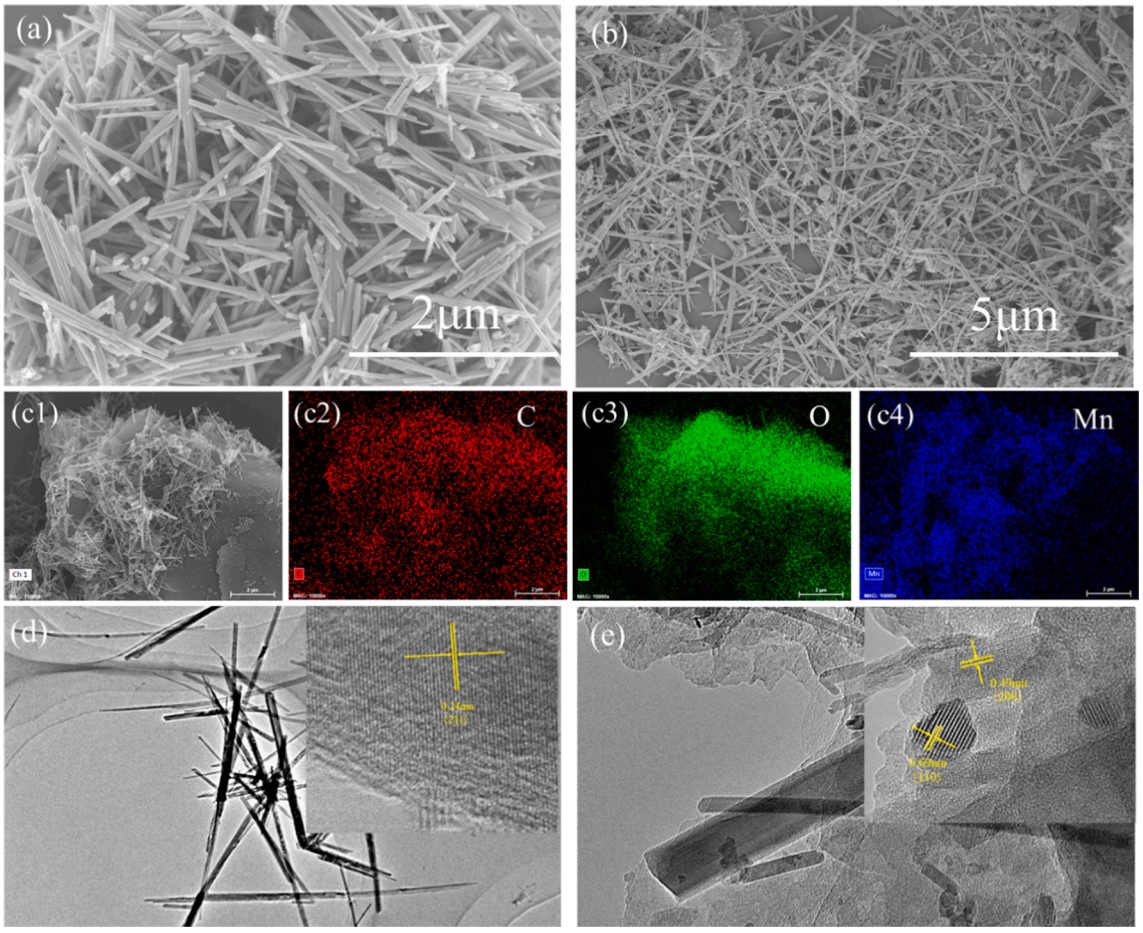

Fig. 2. SEM image of (a) α-MnO_2, (b) α-MnO_2/AC, EDS images of (c1-c4) α-MnO_2/AC and HRTEM images of (d) α-MnO_2 (e) α-MnO_2/AC.

and Fig. S2 (a-c), each of the four crystal phases α-MnO_2, β-MnO_2, γ-MnO_2, and δ-MnO_2 displays distinct morphologies, characterized by needle-like, rod-like, sea urchin-like, and flower-like structures, respectively. As seen in Fig. 2(b) and Fig. S2 (d-f), needle-like α-MnO_2 was uniformly distributed on the surface of AC, sea urchin-like γ-MnO_2 was formed at the holes of AC, and spherical δ-MnO_2 was aggregated and distributed on the surface of AC, this again illustrates the successful preparation of α-MnO_2/AC, γ-MnO_2/AC, and δ-MnO_2/AC. In addition, the MnO_2 loaded on AC was more dispersed and smaller particle size. Unfortunately, in contrast, MnO_x manifests as fragmented rod-shaped particles adhering to the activated carbon (AC) surface, and in conjunction with the XRD analysis above, we believe that β-MnO_2/AC has not yet been successfully synthesized, therefore, we named the material MnOx/AC.

Energy-dispersive X-ray spectroscopy (EDS) mapping in Fig. S3 and Fig. 2(c1-c4) reveals a uniform distribution of Mn, O, and C elements on the surfaces of α-MnO_2/AC, MnOx/AC, γ-MnO_2/AC, and δ-MnO_2/AC, According to high-resolution transmission electron microscopy (HRTEM), well-ordered lattice fringes are clearly visible in both α-MnO_2 and α-MnO_2/AC (Fig. 2(d, e)). As confirmed by JCPDS29-1020 and consistent with XRD data, the lattice spacings of 0.24 nm, 0.49 nm, and 0.69 nm in the point patterns correspond to the interplanar distances of

(211), (200), and (110) crystal planes of α-MnO_2.

Comparison of different materials

The BAA removal efficiency of distinct crystal-phase manganese dioxides is shown in Fig. 3(a). The application of ozone (O_3) alone resulted in a 37.76 % removal rate of BAA within the first 40 min. the BAA degradation sequence by different crystal-phase MnO_2/O_3 follows the order α-MnO_2 (54.55 %) > γ-MnO_2 (51.39 %) > β-MnO_2 (47.19 %) > δ-MnO_2 (42.47 %). Additionally, the pseudo-first-order reaction kinetics model proficiently fits the BAA degradation processes in α-, β-, γ-, and δ-MnO_2/O_3 mediated systems. The calculated pseudo-first-order rate constants of BAA degradation were 0.01897 min^{-1}, 0.01545 min^{-1}, 0.01764 min^{-1}, and 0.01366 min^{-1} for α-, β-, γ-, and δ-MnO_2/O_3, respectively.

The removal of BAA by each composite nanomaterial after loading MnO_2 onto activated carbon was significantly enhanced, and the degradation of BAA by catalytic ozone oxidation of four composite nanomaterials is shown in Fig. 3(b). Among these, α-MnO_2/AC demonstrates the highest BAA degradation efficiency, reaching 84.2 %. For MnO_x/AC, γ-MnO_2/AC, and δ-MnO_2/AC, the BAA degradation efficiencies are 65.8 %, 73.81 %, and 63.46 %, respectively, while AC alone achieves a degradation rate of only 47.7 % under identical experimental setups. Moreover, the pseudo-first-order reaction kinetics model fits BAA's degradation processes catalyzed by α-MnO_2/AC, MnOx/AC, γ-MnO_2/AC, and δ-MnO_2/AC. The calculated pseudo-first-order rate constants are 0.04535 min^{-1}, 0.02742 min^{-1}, 0.03382 min^{-1}, and 0.0254 min^{-1}, respectively. Notably, α-MnO_2 demonstrates the highest degradation rate for BAA among the different crystal phases. Furthermore, α-MnO_2/AC exhibits the highest enhancement in BAA removal rate, reaching 29.61 %. Consequently, α-MnO_2/AC is selected for subsequent experimental investigations.

Fig. 3(c) displays the Raman spectra of α-MnO_2 and α-MnO_2/AC. A distinct Raman peak at 647 cm^{-1} is evident in both α-MnO_2 and α-MnO_2/AC, signifying the characteristic Mn-O vibrations and confirming the presence of Mn-O in the substrates [30,31]. The peak at 1384 cm^{-1} corresponds to the typical D-band, indicating of disordered carbon or defective graphite structures. Further, the peak at 1603 cm^{-1} is attributed to the G-band, providing evidence of the presence of graphite layers [32]. The measured intensity ratio of the ID/IG bands in the α-MnO_2/AC composite is 0.75, signifying a high defect density in composites. The Raman spectra of the remaining materials are shown in Fig. S4. β-MnO_2, γ-MnO_2, δ-MnO_2, γ-MnO_2/AC, and δ-MnO_2/AC similarly showed distinct Mn-O peaks, however, MnOx/AC showed a significant peak shift, which is indicative of the fact that β-MnO_2/AC has not been successfully synthesized.

The IR band at 665 cm^{-1}, observed for both α-MnO_2 and α-MnO_2/AC, is ascribed to Mn-O bending vibrations [33] (Fig. 3(d)). The broadband at 3400 cm^{-1} indicates –OH stretching vibrations of surface hydroxyls or sorbed water [34]. Additionally, the IR band at approximately 1600 cm^{-1} is specific to the bending vibrations of surface hydroxyls [35]. The FTIR spectra of the remaining materials are shown in Fig. S5. Crucially, the characteristic infrared bands of α-MnO_2/AC do not show significant differences after use, indicating the excellent stability of α-MnO_2/AC.

The N_2 adsorption isotherms and pore size distribution of different catalysts are shown in Fig. 3(e), Fig. 3(f), and Fig. S6. α-MnO_2, α-MnO_2/AC, β-MnO_2, MnOx/AC, γ-MnO_2, γ-MnO_2/AC, δ-MnO_2 and δ-MnO_2/AC all exhibit typical type IV isotherms and H3 hysteresis loops, suggesting that the catalysts have mesoporous structures [36]. Table S1 summarizes the specific surface area and pore size distribution of the different catalysts. The average pore diameters for α-MnO_2 and α-MnO_2/AC are 12.348 nm and 3.816 nm, respectively, providing further confirmation of their mesoporous nature. The specific surface area (SBET) of α-MnO_2/AC was 47.205 m^2/g, which was slightly lower than that of α-MnO_2 (83.056 m^2/g). Although the reduced SBET of α-MnO_2/AC may be considered detrimental to the catalytic process, specific interactions between MnO_2 and AC may enhance the catalytic ability, such as by enhancing the dispersion of MnO_2 and reducing the diameter of MnO_2. This is also consistent with the results of the SEM analysis above. Moreover, both catalysts exhibit relatively small pore volumes, indicating that the catalytic reactions predominantly occur on the catalyst's surface rather than within the pores or channels [37].

The interfacial electron transfer rates between α-MnO_2 or α-MnO_2/AC and the solution phase were scrutinized using electrochemical impedance spectroscopy (EIS). In principle, the diameter of the Nyquist

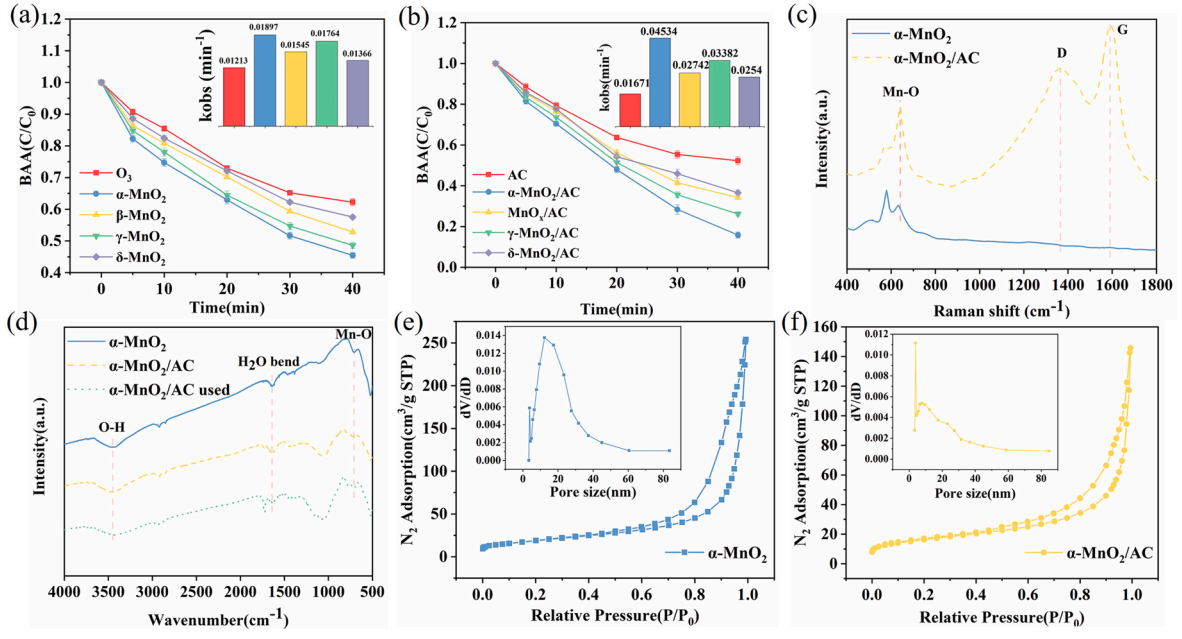

Fig. 3. (a) Degradation of BAA in α-, β-, γ-, and δ-MnO_2/O_3, (b) Degradation of BAA in α-MnO_2/AC, MnOx/AC, γ-MnO_2/AC and δ-MnO_2/AC/O_3, (c) Raman spectra of α-MnO_2 and α-MnO_2/AC, (d) FTIR spectra of α-MnO_2、α-MnO_2/AC and α-MnO_2/AC used, and N_2 adsorption–desorption isotherm of (e) α-MnO_2 and (f) α-MnO_2/AC. Experimental conditions: ([BAA] = 100 mg/L, [ozone] = 5 mg/L, [catalyst] = 0.5 g/L, T = 25℃, pH = 7.0.).

plots' semicircle indicates the strength of polarization resistance [38]. An increase in electrode potential corresponds to an enlargement of the Nyquist semicircle diameter, signaling an elevation in charge transfer resistance [39]. As illustrated in Fig. 4(a), α-MnO_2/AC exhibits a smaller semicircle in the Nyquist plot, suggesting lower polarization resistance and a faster charge transfer rate for α-MnO_2/AC. The electrochemical impedance data of the modified electrode were further analyzed via the equivalent circuit simulation. Table S2 shows the circuit simulation parameters, and the resistances of α-MnO_2 and α-MnO_2/AC are 1119 Ω and 425.3 Ω, respectively. These results confirm that the electrical coordination between MnO and AC in α-MnO_2/AC expedites interfacial electron tra and improves the charge transfer efficiency.

The redox activity of α-MnO_2 and α-MnO_2/AC was characterized using cyclic voltammetry (CV). As shown in Fig. 4(b), the anodic current peaks align with the $Mn^{2+} \rightarrow Mn^{3+}$ to $Mn^{3+} \rightarrow Mn^{4+}$ oxidation, while the cathode current peaks correspond to the $Mn^{4+} \rightarrow Mn^{3+}$ and $Mn^{3+} \rightarrow Mn^{2+}$ reduction. Notably, both the reduction and oxidation curves of α-MnO_2/AC exhibit significantly higher current intensities compared to bare α-MnO_2. This disparity suggests that the Mn in the α-MnO_2/AC carries a high surface charge [40]. Consequently, it can be inferred that α-MnO_2/AC shows exceptional cyclic redox capability, a crucial aspect for restoring the substrate's catalytic activity. The broad CV curves observed for α-MnO_2/AC attributed to the enhanced redox processes facilitated by O_3.

The elements' surface composition and chemical states play a crucial role in catalytic ozonation. The wide-scan XPS spectrum (Fig. 4(c)) observed peaks for C 1 s, O 1 s, Mn 2p, and Mn 3 s in the α-MnO_2/AC catalyst; this shows the presence of Mn and O, corresponding to the previous eds results.

In Fig. 4(d), the Mn $2p_{3/2}$ spectrum can be divided into two peaks located at 641.6 and 642.9 eV, respectively corresponding to the binding energies of Mn^{3+}, and Mn^{4+} [19]. The Mn(III) content on the catalyst surface was α-MnO_2/AC (67.52 %) > α-MnO_2 (62.28 %).The molar ratio of Mn^{3+} and Mn^{4+} was quantified for α-MnO_2/AC (2.08), surpassing that of α-MnO_2 (1.70). The reactivity of the catalysts was positively correlated with the surface Mn(III) content, this suggests that Mn(III) may be the primary active site.

Simultaneously, the average oxidation state (AOS) of Mn species was quantified using Formula 1 (ΔE as the difference in binding energy between the two peaks)[41]. The lower AOS value (3.30) for α-MnO_2/AC (Fig. 4(e)) suggests a higher content of low-valent Mn in α-MnO_2/AC compared to its α-MnO_2 counterpart. It is generally acknowledged that low-valent Mn induces Jahn − Teller distortion, thereby promoting the formation of oxygen vacancies to maintain the charge balance, based on the process shown in Formula 2 [8,42], Oxygen vacancies consistently serve as active sites during the catalytic ozonation.

$$AOS = 8.956 - 1.126\Delta E \quad (1)$$

$$4Mn^{4+} + O^{2-} \rightarrow 4Mn^{4+} + 2e^-/V_0 + 0.5O_2 \rightarrow 2Mn^{4+} + 2Mn^{3+} + V_0 + 0.5O_2 \quad (2)$$

Moreover, the O1s spectrum in Fig. 4(f) is divided into two peaks at 529.8 and 531.5 eV, attributed to lattice oxygen (O_{latt}) and low-coordinated oxygen (O_{ads}) adsorbed on oxygen vacancy sites, respectively [43,44]. Generally, the content of O_{ads} represents the remaining oxygen vacancy sites on the material, as oxygen molecules can adsorb on oxygen vacancies and evolve into O_{ads} on the catalyst surface. The molar ratio of O_{ads} to O_{latt} is as follows: α-MnO_2/AC (7.06) > α-MnO_2 (0.50), indicating the formation of more oxygen vacancy sites on the surface of α-MnO_2/AC, Oxygen vacancies always act as active sites in the catalytic ozonation process [20], therefore compared with α-MnO_2, α-MnO_2/AC is more favourable to catalyze ozone.

Therefore, loading α-MnO_2 on AC can improve its dispersion, reduce the particle size, lower the polarization resistance, and thus increase the charge transfer rate. The electrocoordination of MnO and AC in α-MnO_2/AC accelerates the interfacial electron exchange, the manganese in α-MnO_2/AC has a higher surface charge, which gives it a better redox cycling ability, and the higher Mn(III) and oxygen vacancy content in α-MnO_2/AC, which together contribute to the better ozone oxidation catalytic effect of α-MnO_2/AC.

The influence of experimental conditions on the degradation of BAA

The oxidative degradation efficiency of BAA by the catalyst was optimized as a function of content of AC doping, catalyst dose, ozone concentration, solution pH, temperature, and initial BAA concentration. At a given experiment only one parameter was changed. Unless otherwise specified, the following conditions were kept fixed: 100 mg/L BAA,

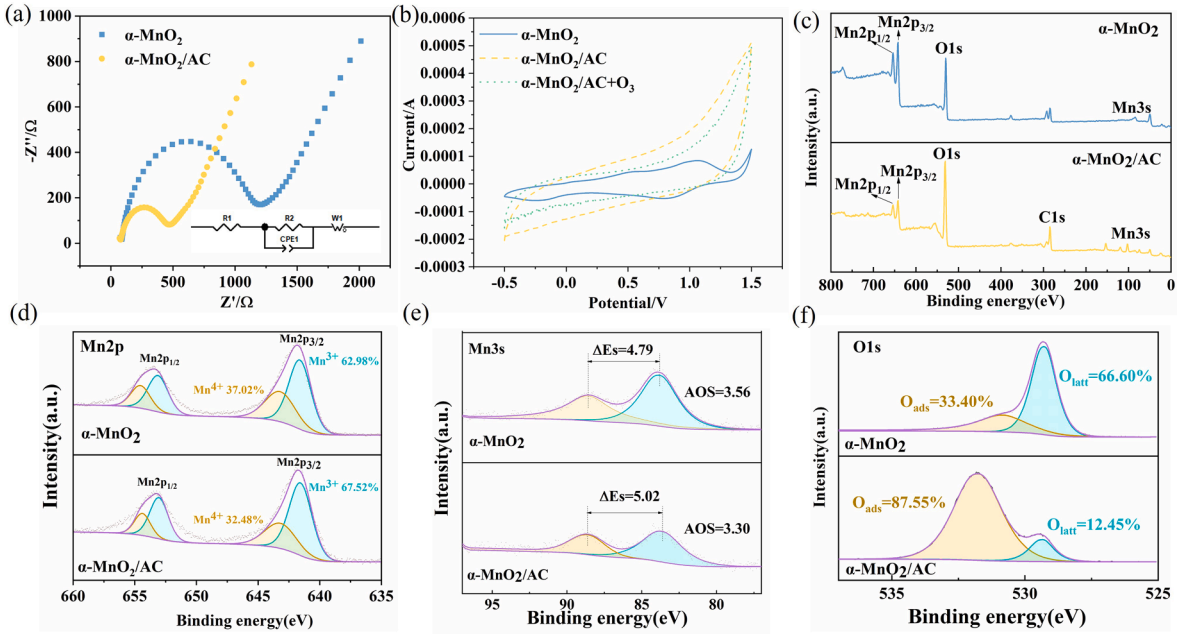

Fig. 4. (a) EIS Nyquist plots of α-MnO_2 and α-MnO_2/AC, (b)CV curves with α-MnO_2、α-MnO_2/AC and O_3/α-MnO_2/AC, (c)XPS survey scan of α-MnO_2 and α-MnO_2/AC XPS high-resolution of (d) Mn 2p, (e) Mn 3 s, (f) O1s.

0.5 g/L catalyst, 5 mg/L ozone concentration, solution pH 7, and a temperature of 25 °C. As depicted in Fig. 5a, the BAA degradation rate steadily increased with AC doping in the range of 0–2 g AC and declined at an excess AC content beyond 2 g. Therefore, 2 g AC was chosen as the optimal amount in subsequent experiments.

As shown in Fig. 5b, the influence of α-MnO_2/AC dosage on BAA degradation was also investigated. With the catalyst content increasing from 0 g/L to 0.75 g/L, the degradation rate of BAA steadily increased as a function of catalyst dose from 37.8 % to 87.8 % within 40 min. However, increasing the dosage of α-MnO_2/AC to 1 g/L did not significantly enhance the BAA degradation efficiency, viz., a 1.01 % increase. Augmenting the catalyst dosage can provide additional active sites for ozone decomposition and reactive oxygen species (ROS) generation. However, excessive catalyst amounts can lead to an instantaneous surplus of ROS due to the fixed concentration of O_3 in the solution. The surplus ROS may react with O_3, itself, or the intermediates of BAA, severely diminishing the likelihood of reactions with BAA [45]. In the process of ozone catalytic oxidation, a dosage of 0.75 g/L for α-MnO_2/AC was identified as optimal. Excessive catalyst dosage not only increases operational costs but also impacts degradation efficiency. Therefore, maintaining the catalyst concentration at the optimum value is crucial for the effective degradation of BAA.

The effect of O_3 concentration on the degradation of BAA by O_3/α-MnO_2/AC is shown in Fig. 5(c). At 2.5 mg/L ozone dosage, the degradation rate of BAA reached 59.7 % within 20 min. Subsequently, increasing the O_3 concentration to 5 mg/L significantly enhanced the BAA degradation efficiency, reaching 87.8 %. However, further elevating the O_3 concentration to 7.5 mg/L and 10 mg/L showed negligible additional improvement (viz., 1.01 %) in the degradation of BAA. Considering operational costs, a dosage of 5 mg/L ozone is deemed sufficient for the effective degradation of BAA in our system.

As illustrated in Fig. 5(d), the solution pH significantly influences the degradation of BAA through catalytic ozonation. In the pH range of 3.00 to 9.00, there is a noticeable increase in the BAA degradation rate. However, beyond pH 9.00, the degradation rate of BAA exhibits a mild increase, possibly attributed to the rapid decomposition of O_3 and termination reactions activated between O_3 and excess •OH radicals (Equations (3)–(5) [46]. [In the pH range of 9.00 to 11.0, BAA predominantly exist in a deprotonated form, facilitating rapid reactions with O_3 [47].

$$\bullet OH + O_3 \rightarrow HO_4^{\bullet} \quad (3)$$

$$HO_4^{\bullet} \rightarrow O_2 + HO_2^{\bullet} \quad (4)$$

$$\bullet OH + HO_2^{\bullet} \rightarrow O_2 + H_2O \quad (5)$$

Fig. 5(e) illustrates the degradation of BAA through ozone catalytic oxidation by α-MnO_2/AC at different reaction temperatures. As the temperature increases from 5 °C to 25 °C, the degradation efficiency of BAA rises from 76.1 % to 96.3 % within 40 min. At 35 °C and 45 °C, there is a slight decrease in BAA degradation efficiency from 93.9 % to 90.3 %. Hence, α-MnO_2/AC, exhibits a wide adaptability window to reaction temperatures. In the final analysis, as shown in Fig. 8(f), we scrutinized the impact of the initial BAA concentration on its degradation efficiency through the influence of α-MnO_2/AC. As revealed in Fig. 5(f), the degradation of BAA initially experiences an upward trend but shows a distinct decline, reaching a threshold value at around BAA 150 mg/L. The observed pattern in BAA degradation by α-MnO_2/AC can be attributed to the limited availability of catalytic sites [7]. Based on the aforementioned experimental results, we have concluded the optimal conditions for the degradation of BAA by O_3/α-MnO_2/AC: initial [BAA] 100 mg/L, [ozone] 5 mg/L, catalyst AC doping amount 2 g, catalyst dose 0.75 g/L, pH 11, and a temperature 25 °C. Under these optimized conditions, the degradation rate of BAA reached 96.3 % and that of TOC reached 67.73 % (Fig. S7.) within 40 min.

Degradation mechanism of α-MnO_2/AC in the ozone catalytic oxidation system

To ascertain the active oxygen species and their contribution to BAA degradation, we conducted radical quenching experiments. Traditional

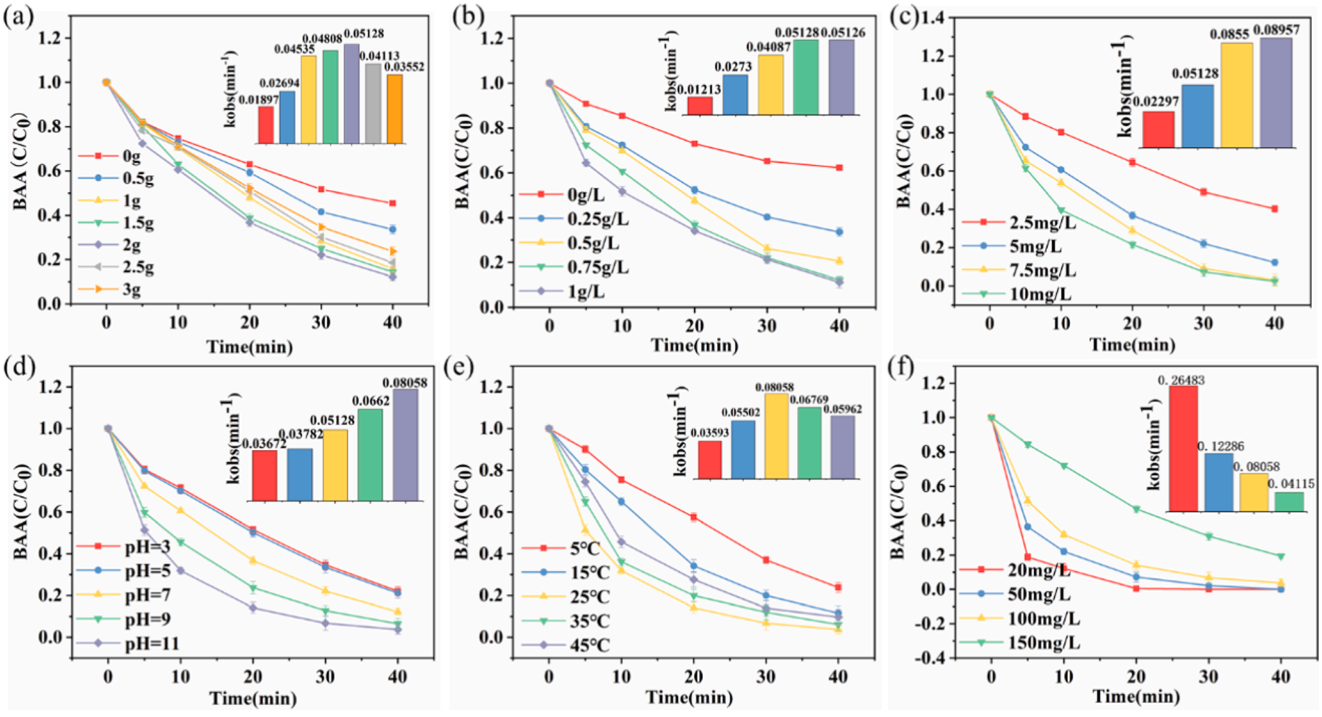

Fig. 5. The effect of operating factors on BAA degradation in the O_3/α-MnO_2/AC system. (a)AC doping amount, (b) The effect of catalyst dosage, (c) ozone dosage, (d) solution pH, (e) temperature, (f)the initial concentration of BAA. Except for the parameters studied, other parameters:([BAA] = 100 mg/L,[ozone] = 5 mg/L, [catalyst] = 0.5 g/L,T = 25℃,pH = 7.0.).

radical quenchers such as TBA (eliminating •OH) [48], p-BQ (eliminating $•O_2^-$) [49] and FFA (eliminating $^1O_2$) [50]. The results are depicted in Fig. 6(a). TBA emerges as a potent scavenger for free •OH radicals. In the presence of 1 mM and 10 mM TBA, the degradation rates of BAA decreased to 90.1 % and 55.6 %, respectively, signifying the predominant role of •OH as the primary ROS. Interestingly, the addition of p-BQ and FFA also significantly suppressed the degradation of BAA. This suggests that in the α-MnO_2/AC ozone catalytic oxidation system, both $•O_2^-$ and $^1O_2$ may coexist. Additionally, FFA exhibited a much higher inhibitory effect on the reaction compared to TBA (42.4 %), with p-BQ showing the lowest inhibition of reactive oxygen species (ROS) (75.7 %). Therefore, it can be hypothesized that ozone is activated to generate ROS such as •OH and $^1O_2$. However, due to the rapid consumption of •OH, ozone, and other ROS by p-BQ or FFA, adding a sufficient amount of p-BQ or FFA (with a concentration exceeding that of BAA) swiftly inhibits the degradation of BAA [37]. We can conclude that $^1O_2$ is also a primary reactive oxygen species (ROS), as evidenced by the fact that the removal rate and kinetic constants of BAA with the three quenching agents are all lower than those with single ozone oxidation. This observation might be attributed to the competition between excess quenching agents and intermediates for O_3 and ROS.

Further validation of the presence of •OH, $•O_2^-$, and $^1O_2$ in the catalytic ozonation was carried out using electron paramagnetic resonance (EPR). In this study, DMPO was employed as a spin-trapping agent for •OH and $•O_2^-$, while TEMP was used as a trapping agent for $^1O_2$. The DMPO-•OH complex (Fig. 6(b)) exhibited characteristic spectra with an intensity ratio of 1:2:2:1 in both the O_3 and O_3/α-MnO_2/AC systems [51]. The characteristic spectra of the TEMP-$^1O_2$ complex (Fig. 6(d)) with an intensity ratio of 1:1:1 were observed in both the O_3 and O_3/α-MnO_2/AC systems [52]. The addition of α-MnO_2/AC catalyst significantly increased the intensity of DMPO-•OH and TEMP-$^1O_2$, leading to the generation of •OH and $^1O_2$. However, the signal intensity of DMPO-$•O_2^-$ (with an intensity ratio of 1:1:1:1) did not show a significant enhancement upon the addition of the α-MnO_2/AC catalyst (Fig. 6(c)) [53], This is consistent with the previous quenching experiments.

These results indicate that O_3 adsorbs on Mn sites (either directly on Mn sites or indirectly on oxygen vacancies) and decomposes in situ into surface •OH and $^1O_2$. In addition, $•O_2^-$ as a selective oxidant contributes relatively less to the degradation of BAA. Therefore, we believe that ·OH, $•O_2^-$, and $^1O_2$ coexist in the α-MnO_2/AC ozone catalytic oxidation, with ·OH and $^1O_2$ being the main ROS in the reaction.

To further examine the active site of the α-MnO_2/AC HCO reaction, we explicitly compared the XPS characterization analysis of fresh and used α-MnO_2/AC, as shown in Fig. S8 (a). The total spectrum of α-MnO_2/AC before and after HCO was essentially unchanged. As depicted in Fig. S8 (b), the C 1 s spectrum of α-MnO_2/AC can be divided into three peaks, attributed to the formation of C–C/C = C (284.6 eV), C-O-C (286.7 eV), and C-O-Mn (288.6 eV) [54–56]. There is minimal change in the C 1 s peaks after the reaction.

As shown in Fig. 6(e), after the α-MnO_2/AC reaction, the catalyst surface Mn^{4+} content decreased from 32.48 % to 30.31 %, the surface Mn^{2+} content increased from 0 to 26.76 %, and the content of Mn^{3+} decreased from 67.52 % to 42.93 %, which, combined with the positive correlation between the catalyst reactivity and the surface MnIII (s) content before, suggests that the active site is electron-rich MnIII (s), which provides electrons to ozone and oxidizes to Mn(IV), which is reduced to Mn(III) via a free radical reaction chain as shown in Eq. ((6)-(8)). Furthermore, during this advanced oxidation process, electrons generated from degraded pollutants can be resupplied to the electron-rich Mn sites [57]. Therefore, the conversion of Mn(III) to Mn(IV) can effectively induce O_3 decomposition and pollutant degradation, and the electrons supplied by degraded pollutants can also effectively promote the conversion of Mn(III) to Mn(II) (Eq.9).

In addition, other active sites (e.g., oxygen vacancies) on the α-MnO_2/AC surface may also promote the generation of HCO. According to previous studies, oxygen vacancies (Vo) are generated to maintain the electrostatic equilibrium once Mn(III) is present in MnO_2[20]. O_{ads} content represents the amount of oxygen vacancies remaining on the material, as oxygen molecules can adsorb at oxygen vacancies and evolve into O_{ads} on the catalyst surface. As shown in Fig. 6(f), the molar

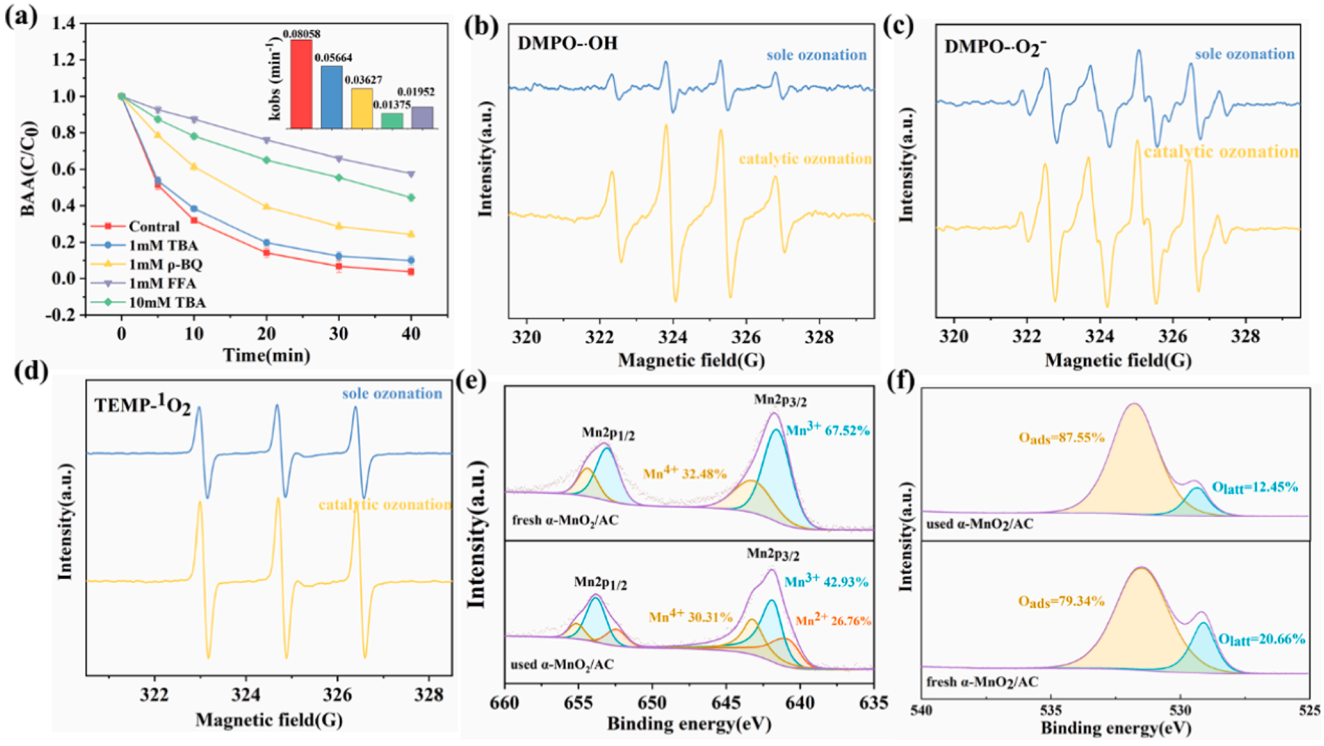

Fig. 6. (a) Effect of TBA, p-BQ and FFA on BAA degradation in O_3 alone and the O_3/α-MnO_2/AC system (b) EPR spectra of DMPO-•OH, (c) DMPO-$•O_2^-$and (d) TEMP-$^1O_2$ in O_3 alone and the O_3/α-MnO_2/AC system, and XPS high-resolution of (e) Mn 2p, (f) O 1 s.

ratio of O_{ads} to O_{latt} decreased from 7.03 to 3.84 after the α-MnO_2/AC reaction, which suggests that Vo acts as an active site for the reaction to promote the generation of HCO. In addition, appropriate concentrations of Vo on the MnO_2 surface can promote interfacial charge transfer [58]. Thus, Vo may play a crucial role in generating ROS from MnO_2-activated O_3. Typically, when O_3 flows over MnO_2, the O_3 molecule replenishes the O vacancy by providing O to bind to the catalyst [23]. Oxygen vacancies have been reported to transfer two electrons to the oxygen atom of O_3 as a two-electron donor, resulting in the desorption of an O_2 molecule into the environment and leaving a reactive oxygen species (O^{2-}) in the O vacancies (Eq.10)[59]. Another O_3 molecule can then react with O^{2-} to form O_2 as well as a bridging O_2 dimer (peroxide, O_2^{2-}) (Eq.11). In addition, the reaction between O^{2-}/O_2^{2-} actives and O_3 can generate other oxygen-containing actives ($\bullet O_2^-/{}^1O_2/\ \bullet OH$) through charge transfer interactions. In these reactions, the oxygen-containing substances gradually accumulate on the α-MnO_2/AC surface while converting to O_2 molecules, releasing a certain amount of oxygen vacancies and maintaining the electrostatic equilibrium.

$$Mn(III) + O_3 + H_2O \rightarrow Mn(IV) + OH^- + \bullet OH + O_2 \quad (6)$$

$$Mn(IV) + \bullet O_2^- \rightarrow Mn(III) + O_2 \quad (7)$$

$$Mn(III) + HO_2^- \rightarrow Mn(II) + H^+ + O_2 \quad (8)$$

$$Mn(III) + e^- \text{ (from BAA)} \rightarrow Mn(II) \quad (9)$$

$$O_3 + Vo \rightarrow O^{2-} + O_2 \quad (10)$$

$$O^{2-} + O_3 \rightarrow O_2^{2-} + O_2 \quad (11)$$

$$O^{2-} \rightarrow O_2 + Vo \quad (12)$$

$$O^{2-}/O_2^{2-} + H_2O \rightarrow \bullet O_2^- / {}^1O_2 / \bullet OH \quad (13)$$

$$BAA + {}^1O_2 / \bullet OH \rightarrow \text{intermediates} + CO_2 + H_2O + e^- \quad (14)$$

Based on the available data, a potential degradation mechanism for α-MnO_2/AC catalyzed ozone oxidation of BAA was proposed (Fig. 7). Conversion of Mn(III) to Mn(IV) can effectively induce O_3 catabolism into ROS for BAA degradation. At the same time, electrons provided by degraded pollutants can also effectively promote the conversion of Mn (IV) to Mn(III). At the same time, O_3 can be trapped and decomposed by structural defects (Vo, mainly oxygen vacancies) on the MnO_2 surface and then converted to reactive oxygen species ($O^{2-}/\ O_2^{2-}$), which rapidly evolve via chain-cycle reactions to $\bullet O_2^-/\bullet OH/{}^1O_2$(Eq.12–13). These defects can be regenerated by cycling, thus maintaining long-term removal efficiency. Overall, O_3 is activated at the active sites Mn(III) and Vo to generate ROS; the reactive radical •OH and $^1O_2$ reacts with the BAA molecule, leading to the mineralization of BAA into CO_2, H_2O and inorganic ions.

Degradation pathway of BAA

The LC-MS mass spectroscopic details of the BAA intermediates after O_3/α-MnO_2/AC induced catalytic degradation are shown in Fig. S9 and Table S3. Based on the mass spectroscopic data, We deduced two possible degradation pathways for BAA as shown in Fig. 8.

Pathway 1: Generally, ·OH attacks organic compounds through processes such as electron transfer, hydrogen abstraction, and ·OH electrophilic addition to double bonds. Compound 1 is formed by the oxidation of the –NH_2 group. The aromatic ring of Compound 1 undergoes initial cleavage to form Compounds 3 and 6. Subsequently, Compound 3 transforms into Compound 4, and Compound 4 further converts into Compound 5 [60].

Pathway 2: The formation of Compound 2 results from the cleavage of the C-Br bond and hydroxylation. Subsequently, free radicals attack Compound 2, leading to the generation of Compound 7, which is further oxidized to form Compounds 8, 10, and 11. Next, Compounds 10 and 11 undergo oxidation to yield Compounds 12 and 13. Following this, benzene compounds such as phenol and hydroquinone continue to be attacked by free radicals, leading to ring-opening reactions and the generation of small organic acids, including Compound 9. Over an extended period, these organic carboxylic acids undergo further degradation, mineralizing into CO_2 and H_2O.

Toxicity evaluation of BAA and its intermediates in the system

There is considerable research on the computational analysis of intermediates generated during the degradation of bromamine acid, yet investigations into its potential toxic risks are limited. This calls for our attention. Consequently, we employed the T.E.S.T. method to assess the mutagenicity and developmental toxicity of both BAA and its degradation intermediates [61]. As shown in Fig. 9, developmental toxicity refers to the extrapolated toxicity of chemical substances on humans and animals, encompassing any impacts on normal development, both pre-

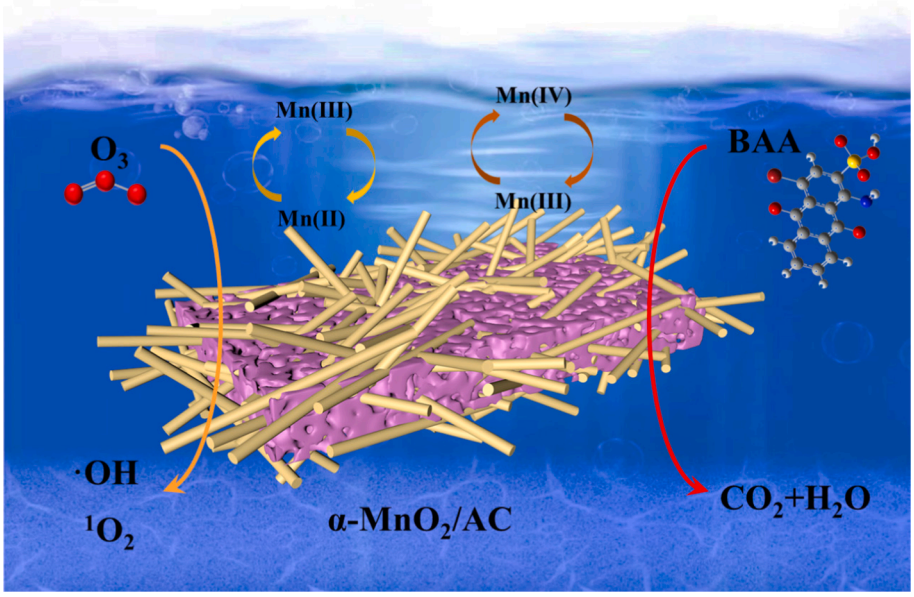

Fig. 7. Schematic diagram of degradation mechanism.

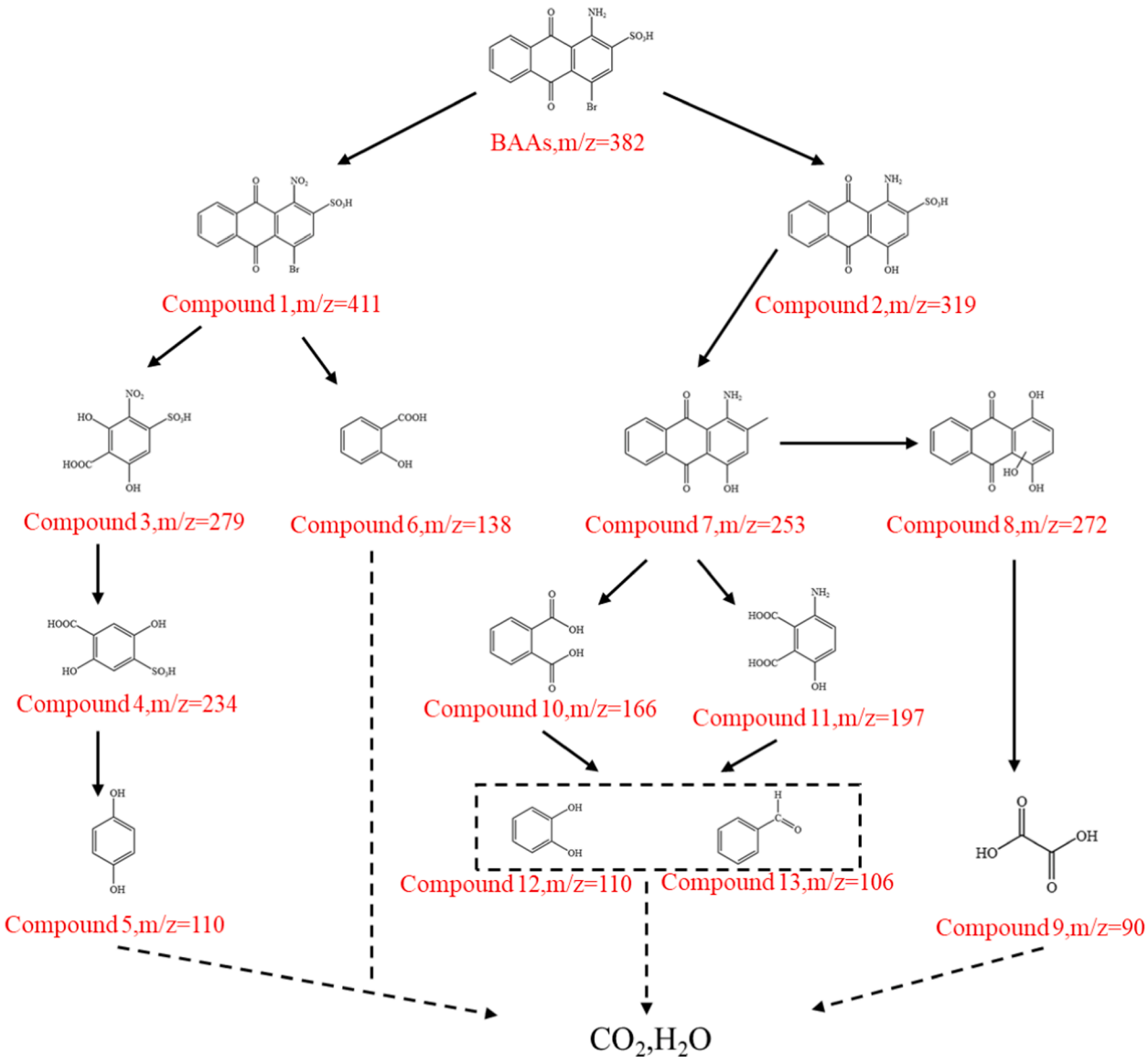

Fig. 8. Degradation pathways and intermediates of BAA in the O_3/α-MnO_2/AC system.

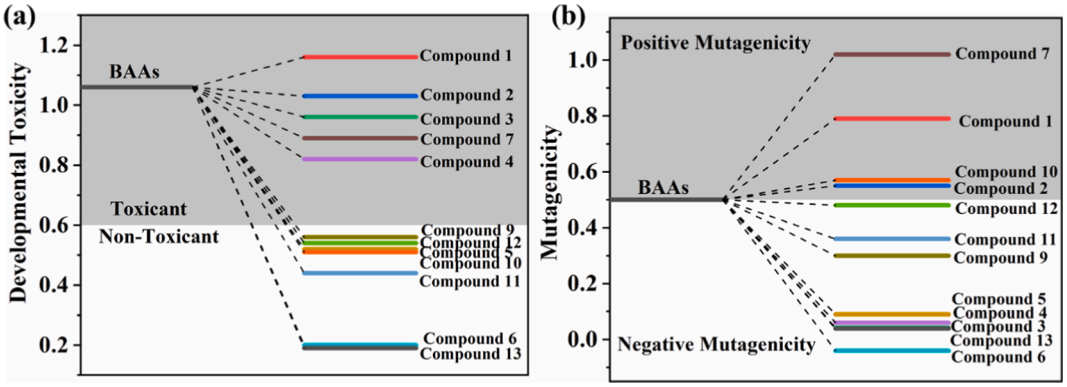

Fig. 9. (a) Developmental toxicity and (b) mutagenicity of BAA and its degradation intermediates in the O_3/α-MnO_2/AC system.

and postnatally. The results indicate that, except for compound 1, the developmental toxicity of the remaining intermediates is lower than that of BAA. Compounds (5, 6, 9–13) are found to be non-toxic. The threshold between positive mutagenicity and negative is indicated by the coefficient of 0.5 [62]. Therefore, in terms of mutagenicity, except for compounds (1, 2, 7, 10), BAA and most of its intermediates are classified as negative mutagenic. In the O_3/α-MnO_2/AC system, the final products of BAA pose a lower environmental risk.

Applications and stability of α-MnO_2/AC

Various types of inorganic anions are present in water and wastewater; these anions can inhibit the degradation of pollutants in the ozone oxidation by competitively interacting with •OH [63,64]. Various common anions (CO_3^{2-}, HCO_3^-, Cl^-, PO_4^{3-}, NO_3^-, and SO_4^{2-}, each at a concentration of 10 mM) were individually introduced into the α-MnO_2/AC-catalyzed ozone oxidation of BAA. Fig. 10a illustrates the degradation of BAA and the pseudo-first-order kinetics. It is observed that anions exhibit a slight inhibitory effect on the catalytic degradation of BAA, with the inhibitory effect ranking as follows: Cl^- > NO_3^- > PO_4^{3-} > HCO_3^- > SO_4^{2-} > CO_3^{2-} and the degradation efficiency was reduced by 22.2 %, 11.9 %, 8.3 %, 5.3 %, 1.7 %, and 1.3 %, respectively.

To further assess the practical performance of the α-MnO_2/AC system, we investigated the influence of different water matrices (deionized water, municipal water supply, Hubing Tang water (a lake within the city), and wastewater from 359) on the removal efficiency of BAA to simulate real-world application scenarios. The physicochemical parameters of lake water and 359 wastewater were presented in Table S4. As shown in Fig. 10b, compared to pure water, the removal efficiency of BAA slightly decreased in 359 wastewater (72.4 %). However, this decline may be attributed to the complexity of the actual water matrix, where various oxidants preferentially oxidize other substances, resulting in a reduced degradation rate of BAA in the actual water sample [65]. The degradation efficiencies of BAA in municipal water supply and Hubing Tang water were 98.2 % and 93.3 %, respectively, closely resembling the degradation efficiency in deionized water (96.3 %), indicating minimal impact on the system. These results suggest that the α-MnO_2/AC system is feasible for practical wastewater treatment applications.

Table S5. summarizes the performance of some catalysts reported in recent years for the degradation of anthraquinone dyes. Compared with other studies, the α-MnO_2/AC catalyst prepared in this study showed higher degradation efficiency and shorter degradation time. This indicates that our synthesized α-MnO_2/AC catalyst is an efficient catalyst.

Additionally, the reusability and stability of α-MnO_2/AC were investigated. As depicted in Fig. 10 (c, d), α-MnO_2/AC demonstrated effective degradation of BAA over five reuse cycles. Moreover, the leaching of Mn from α-MnO_2/AC remained low, measuring only 0.2536 mg/L. This result indicates the excellent stability of α-MnO_2/AC.

Conclusions

Different novel composite nanomaterials were successfully prepared by loading different crystalline phases of manganese dioxide on activated carbon using hydrothermal synthesis-calcination method. Among them, α-MnO_2/AC degraded 100 mg/L BAA up to 96.27 % in 40 min under the optimal conditions of ozone concentration of 5 mg/L, catalyst AC doping of 2 g, catalyst dosage of 0.75 g/L, pH = 11, and temperature of 25 °C. The increase in the dispersion of MnO_2 on α- MnO_2/AC, the α-MnO_2/AC decreased polarization resistance, and increased content of Mn^{3+} and oxygen vacancies were the main reasons for the better ozone oxidation catalytic effect of α- MnO_2/AC. In addition, α- MnO_2/AC exhibited excellent stability and recyclability. The degradation mechanism was also analyzed. Mn(III) and oxygen vacancies on α-MnO_2/AC together acted as active sites to enable O_3 adsorption and activation to produce ROS. •OH and $^1O_2$, as the main active ROS of the α- MnO_2/AC/O_3 system, reacted with the BAA molecules to degrade BAA and the intermediates produced by the reaction had a low The intermediates produced by the reaction have low environmental risks. This study provides a new idea for the design of a novel highly efficient catalytic ozone generator and a new insight into the catalytic mechanism of the HCO process.

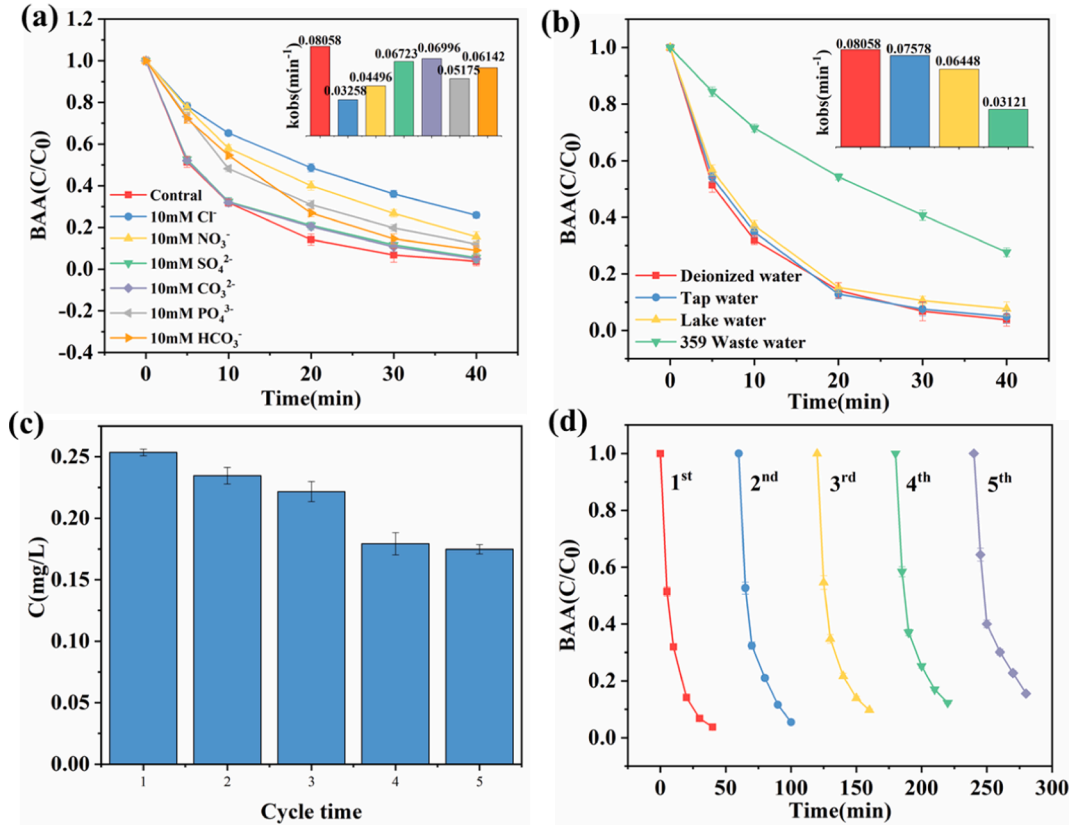

Fig. 10. Effects of (a) inorganic anion, (b) different water matrixes on BAA degradation in O_3/α-MnO_2/AC.(c) Catalytic property of α-MnO_2/AC for repeated use, (d) the leaching of metal ions in the consecutive cycles.

CRediT authorship contribution statement

Cheng Gong: Conceptualization, Formal analysis, Investigation, Methodology, Software, Validation, Visualization, Writing – original draft. **Xinxin Lv:** Investigation, Methodology, Writing – review & editing. **Sheng Liu:** Investigation, Writing – review & editing. **Xing Chen:** Conceptualization, Funding acquisition, Investigation, Project administration, Supervision, Writing – review & editing. **Rohan Weerasooriya:** Conceptualization, Writing – review & editing. **Zhaogang Ding:** Investigation, Supervision, Writing – review & editing.

Declaration of Competing Interest

The authors declare that they have no known competing financial interests or personal relationships that could have appeared to influence the work reported in this paper.

Acknowledgement

The authors acknowledge the financial support from the Key Science and Technology Projects of Anhui Province (202003a07020004), and National Key R&D Program of China (2019YFC0408500).

Appendix A. Supplementary data

Supplementary data to this article can be found online at https://doi.org/10.1016/j.jiec.2024.06.044.

References

[1] L. Huang, G. Sun, T. Yang, B. Zhang, Y. He, X. Wang, Desalination 309 (2013) 91–96.
[2] T. Lu, Q. Zhang, S. Yao, Chin. J. Chem. Eng. 25 (2017) 330–337.
[3] M. Becelic-Tomin, B. Dalmacija, L. Rajic, D. Tomasevic, D. Kerkez, M. Watson, M. Prica, Sci. World J. 2014 (2014) 1–8.
[4] E. Routoula, S.V. Patwardhan, Environ. Sci. Tech. 54 (2020) 647–664.
[5] R. Pelalak, R. Alizadeh, E. Ghareshabani, J. Hazard. Mater. 392 (2020) 122269.
[6] R. Pelalak, R. Alizadeh, E. Ghareshabani, Z. Heidari, Sci. Total Environ. 734 (2020) 139446.
[7] X. Chen, F. Deng, X. Liu, K.-P. Cui, R. Weerasooriya, Sci. Total Environ. 774 (2021) 145776.
[8] J. Jia, P. Zhang, L. Chen, Appl Catal B 189 (2016) 210–218.
[9] Y. Yuan, G. Xing, S. Garg, J. Ma, X. Kong, P. Dai, T.D. Waite, Water Res. 177 (2020) 115785.
[10] F. Nawaz, H. Cao, Y. Xie, J. Xiao, Y. Chen, Z.A. Ghazi, Chemosphere 168 (2017) 1457–1466.
[11] T. Zhang, W. Chen, J. Ma, Z. Qiang, Water Res. 42 (2008) 3651–3658.
[12] A. Mashayekh-Salehi, G. Moussavi, K. Yaghmaeian, Chem. Eng. J. 310 (2017) 157–169.
[13] L. Jothinathan, J. Hu, Water Res. 134 (2018) 63–73.
[14] J. Zhang, B. Xin, C. Shan, W. Zhang, D.D. Dionysiou, B. Pan, Appl. Catal. B 292 (2021) 14215.
[15] C. Chen, X. Yan, Y. Xu, B.A. Yoza, X. Wang, Y. Kou, H. Ye, Q. Wang, Q.X. Li, Sci. Total Environ. 651 (2019) 2631–2640.
[16] Y. Wang, N. Ren, J. Xi, Y. Liu, T. Kong, C. Chen, Y. Xie, X. Duan, S. Wang, ACS ES&T Eng. 1 (2020) 32–45.
[17] K.Z. Huang, H. Zhang, Environ. Sci. Tech. 53 (2019) 12610–12620.
[18] E. Saputra, S. Muhammad, H. Sun, H.M. Ang, M.O. Tadé, S. Wang, Environ. Sci. Tech. 47 (2013) 5882–5887.
[19] F. Wang, H. Dai, J. Deng, G. Bai, K. Ji, Y. Liu, Environ. Sci. Tech. 46 (2012) 4034–4041.
[20] Z. Wang, H. Jia, T. Zheng, Y. Dai, C. Zhang, X. Guo, T. Wang, L. Zhu, Appl Catal B 272 (2020) 119030.
[21] B. Zhao, R. Ran, X. Wu, D. Weng, Appl. Catal. A 514 (2016) 24–34.
[22] W. Yang, Z.a. Su, Z. Xu, W. Yang, Y. Peng, J. Li, Appl. Catal. B: Environ., 260 (2020) 118150.
[23] J. Huang, S. Zhong, Y. Dai, C.-C. Liu, H. Zhang, Environ. Sci. Tech. 52 (2018) 11309–11318.
[24] S.-Q. Tian, J.-Y. Qi, Y.-P. Wang, Y.-L. Liu, L. Wang, J. Ma, Water Res. 193 (2021) 116860.
[25] J. Xu, Y. Li, M. Qian, J. Pan, J. Ding, B. Guan, Appl Catal B 256 (2019) 117797.
[26] S. Shen, X. Zhou, Q. Zhao, W. Jiang, J. Wang, L. He, Y. Ma, L. Yang, Z. Chen, J. Hazard. Mater. 439 (2022) 129613.
[27] X. Xiao, Z. Zhang, Y. Wu, J. Xu, X. Gao, R. Xu, W. Huang, Y. Ye, S.T. Oyakhire, P. Zhang, B. Chen, E. Cevik, S.M. Asiri, A. Bozkurt, K. Amine, Y. Cui, Adv. Mater. 35 (2023) 2211555.
[28] J. Huang, Y. Dai, K. Singewald, C.-C. Liu, S. Saxena, H. Zhang, Chem. Eng. J. 370 (2019) 906–915.
[29] E. Saputra, S. Muhammad, H. Sun, H.-M. Ang, M.O. Tadé, S. Wang, Appl Catal B 142–143 (2013) 729–735.
[30] G. Zhu, L. Wang, H. Lin, L. Ma, P. Zhao, Y. Hu, T. Chen, R. Chen, Y. Wang, Z. Tie, J. Liu, Z. Jin, Adv. Funct. Mater. 28 (2018) 1800003.
[31] Y. Feng, S. Long, G. Yan, B. Chen, J. Sperry, W. Xu, Y. Sun, X. Tang, X. Zeng, L. Lin, J. Catal. 389 (2020) 157–165.
[32] C. Yang, Q. Gao, W. Tian, Y. Tan, T. Zhang, K. Yang, L. Zhu, J. Mater. Chem. A 2 (2014) 19975–19982.
[33] Y. Wang, W. Zhong, S. Zhang, X. Zhang, C. Zhu, X. Zhang, X. Zhang, Y. Chen, Carbon 188 (2022) 254–264.
[34] X. Qi, F. Xie, Chem. Eng. J. 351 (2018) 22–30.
[35] P. Hu, H. Su, Z. Chen, C. Yu, Q. Li, B. Zhou, P.J.J. Alvarez, M. Long, Environ. Sci. Tech. 51 (2017) 11288–11296.
[36] Y. Wang, S. Indrawirawan, X. Duan, H. Sun, H.M. Ang, M.O. Tadé, S. Wang, Chem. Eng. J. 266 (2015) 12–20.
[37] D. Wang, Y. He, Y. Chen, F. Yang, Z. He, T. Zeng, X. Lu, L. Wang, S. Song, J. Ma, Water Res. 230 (2023) 119574.
[38] B. Ruiz-Camacho, J.C. Baltazar Vera, A. Medina-Ramírez, R. Fuentes-Ramírez, G. Carreño-Aguilera, Int. J. Hydrogen Energy 42 (2017) 30364–30373.
[39] R.K. Singh, R. Devivaraprasad, T. Kar, A. Chakraborty, M. Neergat, J. Electrochem. Soc. 162 (2015) F489–F498.
[40] D. Xia, W. Xu, Y. Wang, J. Yang, Y. Huang, L. Hu, C. He, D. Shu, D.Y.C. Leung, Z. Pang, Environ. Sci. Tech. 52 (2018) 13399–13409.
[41] C. He, Y. Wang, Z. Li, Y. Huang, Y. Liao, D. Xia, S. Lee, Environ. Sci. Tech. 54 (2020) 12771–12783.
[42] X. Xie, Y. Li, Z.-Q. Liu, M. Haruta, W. Shen, Nature 458 (2009) 746–749.
[43] T. Mathew, K. Suzuki, Y. Ikuta, N. Takahashi, H. Shinjoh, Chem. Commun. 48 (2012) (1989) 11987.
[44] J. Wang, D. Li, P. Li, P. Zhang, Q. Xu, J. Yu, RSC Adv. 5 (2015) 100434–100442.
[45] H. Chen, J. Wang, J. Hazard. Mater. 403 (2021) 123697.
[46] Y. Liu, D. Wu, S. Peng, Y. Feng, Z. Liu, Sep. Purif. Technol. 209 (2019) 588–597.
[47] F.J. Benitez, J.L. Acero, F.J. Real, G. Roldán, E. Rodríguez, J. Hazard. Mater. 282 (2015) 224–232.
[48] M. Luo, H. Zhou, P. Zhou, L. Lai, W. Liu, Z. Ao, G. Yao, H. Zhang, B. Lai, Water Res. 203 (2021) 117548.
[49] Z. Zhao, W. Zhou, D. Lin, L. Zhu, B. Xing, Z. Liu, Appl Catal B 309 (2022) 121256.
[50] Y. Wang, X. Duan, Y. Xie, H. Sun, S. Wang, ACS Catal. 10 (2020) 13383–13414.
[51] C. Zhou, P. Zhou, M. Sun, Y. Liu, H. Zhang, Z. Xiong, J. Liang, X. Duan, B. Lai, Water Res. 210 (2022) 117984.
[52] L. Xu, B. Fu, Y. Sun, P. Jin, X. Bai, X. Jin, X. Shi, Y. Wang, S. Nie, Chem. Eng. J. 400 (2020) 125870.
[53] Z. Song, Y. Zhang, C. Liu, B. Xu, F. Qi, D. Yuan, S. Pu, Chem. Eng. J. 357 (2019) 655–666.
[54] Y. Xiao, X. Wang, W. Wang, D. Zhao, M. Cao, ACS Appl. Mater. Interfaces 6 (2014) 2051–2058.
[55] L. Zhang, D. Ge, G. Qu, J. Zheng, X. Cao, H. Gu, Nanoscale 9 (2017) 5451–5457.
[56] L. Chen, F. Chen, Y. Shi, J. Zhang, J. Phys. Chem. C 116 (2012) 8579–8586.
[57] L. Lyu, C. Lu, Y. Sun, W. Cao, T. Gao, C. Hu, Appl Catal B 320 (2023) 121871.
[58] Y. Deng, P. Gao, L. Wang, Y. Zhang, J. Fu, R. Huang, S. Zhao, G. Wang, Y. Wei, S. Zhou, J. Environ. Chem. Eng. 10 (2022) 107481.
[59] D. He, G. Wan, H. Hao, D. Chen, J. Lu, L. Zhang, F. Liu, L. Zhong, S. He, Y. Luo, Chem. Eng. J. 289 (2016) 161–169.
[60] L. Liu, J. Zhang, Y. Tan, Y. Jiang, M. Hu, S. Li, Q. Zhai, Chem. Eng. J. 244 (2014) 9–18.
[61] Y. Zhou, J. He, J. Lu, Y. Liu, Y. Zhou, Chin. Chem. Lett. 31 (2020) 2623–2626.
[62] J. Lu, T. Wang, Y. Zhou, C. Cui, Z. Ao, Y. Zhou, J. Hazard. Mater. 383 (2020) 121133.
[63] C. Ouyang, K. Wei, X. Huang, M. Gamal El-Din, X. Zhang, Environ. Sci. Tech. 55 (2021) 11236–11244.
[64] Y. Zhang, H. Ji, W. Liu, Z. Wang, Z. Song, Y. Wang, C. Liu, B. Xu, F. Qi, Sci. Total Environ. 727 (2020) 138696.
[65] X. Lv, H. Liu, Y. Liu, X. Chen, Sep. Purif. Technol. 343 (2024) 127090.